Journal of Radiation Research, Vol. 63, No. 6, 2022, pp. 828–837
https://doi.org/10.1093/jrr/rrac051
Advance Access Publication: 16 September 2022

Prediction of proton beam range in phantom with metals based on monochromatic energy CT images

Qianqian Meng[1], Jing Li[1], Wei Jiang[2,3], Birong Hu[4], Feng Xu[5], Xiaomeng Shi[6] and Renming Zhong[1,*]

[1]Radiophysical Technology Center, Cancer Center, West China Hospital, Sichuan University, Chengdu, 610041, China
[2]Department of Radiotherapy, Yantai Yuhuangding Hospital, Yantai, 264000, China
[3]Academy of Medical Engineering and Translational Medicine, Department of Biomedical Engineering, School of Precision Instrument and Opto-electronics Engineering, Tianjin University, Tianjin, 300072, China
[4]Department of Radiotherapy, Chengdu Second People's Hospital, Chengdu, 610021, China
[5]Lung Cancer Center & Institute, West China Hospital, Sichuan University, Chengdu, 610041, China
[6]CT Imaging Research Center, GE Healthcare China, Shanghai, 201203, China
*Corresponding author. Department of Radiotherapy, Division of Radiation Physics, State Key Laboratory of Biotherapy and Cancer Center, West China Hospital, Sichuan University, Chengdu 610041, P.R. China. Tel: +8628-85422568, E-mail: zrm_100@163.com.
(Received 1 April 2022; revised 30 May 2022; editorial decision 1 August 2022)

ABSTRACT

The purpose of the study was to evaluate the accuracy of monochromatic energy (MonoE) computed tomography (CT) images reconstructed by spectral CT in predicting the stopping power ratio (SPR_w) of materials in the presence of metal. The CIRS062 phantom was scanned three times using spectral CT. In the first scan, a solid water insert was placed at the center of the phantom ($CT_{no\ metal}$). In the second scan, the solid water insert was replaced with a titanium alloy femoral head (CT_{metal}). The metal artifact reduction (MAR) algorithm was used in the last scan ($CT_{metal+MAR}$). The MonoE-CT images of 40 keV and 80 keV were reconstructed. Finally, the single-energy CT method (SECT) and the dual-energy CT method (DECT) were used to calculate the SPR_w. The mean absolute error (MAE) of the SPR_w of the inner layer inserts calculated by the SECT method were 3.19%, 13.88% and 2.71%, corresponding to $CT_{no\ metal}$, CT_{metal} and $CT_{metal+MAR}$, respectively. For the outer layer inserts, the MAE of SPR_w were 3.43%, 5.42% and 2.99%, respectively. Using the DECT method, the MAE of the SPR_w of the inner layer inserts was 1.30%, 3.69% and 1.46% and the MAE of the outer layer inserts– was 1.34%, 1.36% and 1.05%. The studies shows that, compared with the SECT method, the accuracy of the DECT method in predicting the SPR_w of a material is more robust to the presence of metal. Using the MAR algorithm when performing CT scans can further improve the accuracy of predicting the SPR of materials in the presence of metal.

Keywords: metal artifacts; dual-energy computed tomography (DECT); proton range; metal artifact reduction (MAR)

INTRODUCTION

Proton and carbon-ion radiotherapy has become increasingly popular worldwide owing to its physical properties, which can deposit most of the dose to the end of the range and the corresponding sharp dose fall-off beyond the Bragg peak. However, many medical implants contain metals, such as hip and knee replacements, surgical clips and dental filling [1]. This will result metal artifacts [2–4], which reduces the accuracy in dose calculation in radiotherapy [5, 6]. Therefore, it is essential to accurately estimate the range of the particle beam in the human body before treatment. To reduce the impact of metal implants on the quality of computed tomography (CT) images, different commercial CT metal artifact reduction (MAR) algorithms [7–9] was developed.

In the current proton therapy planning system, the conversion curve between the CT numbers (measured in Hounsfield Units [HU]) and the stopping power ratios (SPR_w) is mainly used to estimate the range of proton beams in the patient (single-energy computed tomography [SECT]) [10]. Studies have shown that the uncertainty of the proton range was 3.5% due to the conversion from CT numbers to SPR_w [11, 12] (lack of a one-to-one correspondence between the

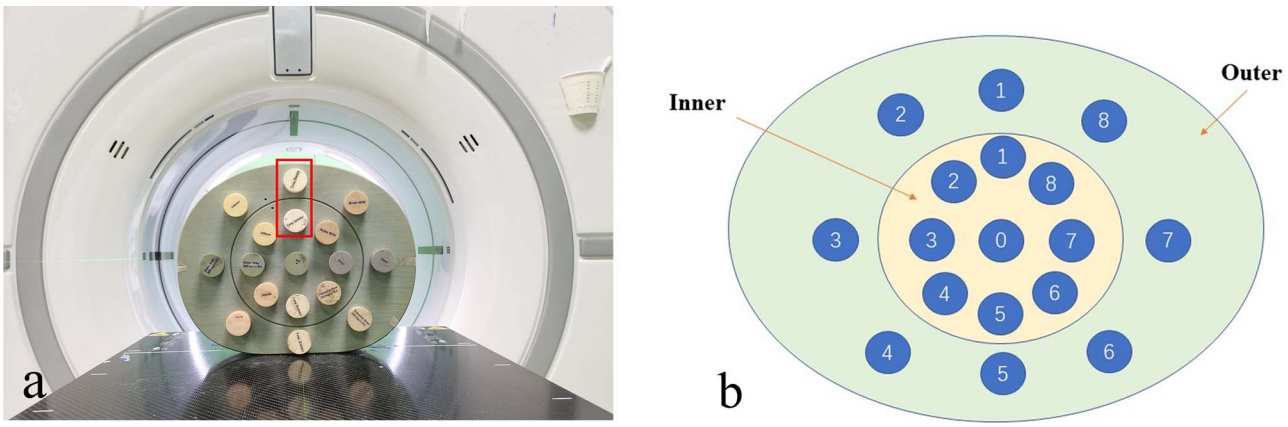

Fig. 1. a. CIRS062 phantom, the materials of the two inserts in the red box are the same. b. Schematic diagram of the CIRS062 phantom, and the numbers represent the different tissue equivalent materials: 0-Solid Water/Metal, 1- Lung (Inhale), 2-Adipose, 3- Dense Bone 800 mg/cc HA, 4- Muscle, 5- Lung (Exhale), 6- Trabecular Bone 200 mg/cc HA, 7- Liver and 8- Breast50/50.

photon attenuation coefficient and the proton stopping power [13]). Many studies have proven that dual-energy CT (DECT) can effectively reduce this estimation error [13–16].

Recently, some researchers have found that the reconstruction of monochromatic energy images (MonoE) by spectral CT can reduce metal artifacts [17–19]. The spectral CT can be achieved by various techniques, such as rapid kVp switching (80 and 140 kVp) [20], dual source [21] and detector or dual-layer detector [22]. The synthetic MonoE can be used to reduce beam hardening artifacts [5]. In addition, the MAR technique can be used to further correct the image affected by the metal artifact [23, 24]. To the best of the authors' knowledge, there are no published reports evaluating the impact of metal implants on the prediction of the proton range. In this article, we used the GE Revolution CT Gemstone Spectral Imaging (GSI) mode to scan the CIRS062 electron density phantom [25] (Norfolk, Virginia 23 513. USA) under three different conditions to study the impact of metal implants on proton range prediction: (i) in the absence of metal ($CT_{no\ metal}$), (ii) in the presence of metal (CT_{metal}), and (iii) in the presence of metal, scanning with the MAR algorithm ($CT_{metal+MAR}$).

MATERIALS AND METHODS

Electron density phantom

Two phantoms containing plastics and epoxy resin-based tissue substitutes were employed as the test objects in this study. One phantom was a Gammex467 tissue characterization phantom (Gammex Inc., Middleton, WI). It is a 33 cm diameter cylinder made of Solid Water [26] with 16 2.8 cm holes that are stuffed with rod-shaped tissue substitute inserts, such as lung, liver, cortical bone, inner bone, brain, adipose, breast [27, 28]. Gammex467 is the calibration phantom in our work. The research phantom was CIRS062. It consists of nested disks made from plastic water and eight different tissue equivalent inserts positioned at 17 different locations. Each plug measures 3.0 cm in diameter and 5.0 cm in length. There is a hole in the center of the CIRS062 phantom. A solid water insert was placed during normal scanning, and a 2.0 cm diameter hemispherical titanium alloy femoral head was placed when evaluating the impact of metal implants. The degree of impact of metal artifacts is related to the distance between the metal inserts. Therefore, we divided the tissue equivalent materials of the CIRS062 phantom into two parts: the inner layer and the outer layer. The tissue equivalent materials at the corresponding positions of the inner and the outer layers were the same, as shsown in the red box in Fig. 1a. Figure 1b shows the specific positions of the tissue equivalent materials in the phantom.

Scanning parameters and reconstruction

The GSI Xtream on GE Revolution™ CT is the first volume spectral CT technology to improve tissue characterization and MAR. The phantom scans were divided into three groups: (1) $CT_{no\ metal}$, the CT scan of CIRS062 phantom without metal, including 120 kVp and reconstructed MonoE-40 keV and MonoE-80 keV CT images. (2) CT_{metal}, the CT scan of phantom with metal and the central insert was replaced by the femoral head of titanium alloy. (3) $CT_{metal+MAR}$, the CT scan using MAR mode. Conventional CT scans used the following parameters: collimation 129 × 0.625 mm, tube voltage 120 kVp, tube current 195 mA and CTDIvol 15.54 mGy. GSI mode was collimation 129 × 0.625 mm, tube voltage 80 kVp/140 kVp instantaneous switching, mA mode of GSI assist and CTDIvol 10.91 mGy. Images were reconstructed with and without MAR mode [29]. The pitch was 0.508:1, the FOV was 50 cm, and the rotation time was 0.6 s. We reconstructed CT images of 120 kVp, which are commonly used in clinical practice, under conventional scanning. Meanwhile, the images of MonoE-40 and -80 keV were reconstructed using GSI scan mode.

Two SPR_w calculation methods

Single-energy computer tomography method

This is similar to the electron density calibration curve in photon radiotherapy. Using a single energy X-ray to predict the SPR of a material is used to establish a calibration curve between CT HUs and the stopping power ratio (SPR) to water. Table 1 shows the element composition information of the two phantoms. The relative electron density (ρ_e), mean excitation energy for mixture (I) and SPR (SPR_w) of tissue

Table 1. Mass density and elemental composition of the inserts employed in Gammex467 and CIRS062, provided by manufacturer

Materials		p*	H	C	N	O	Ba	Mg	Si	P	Cl	Ca
LN300	Gammax467	0.30	8.46	59.37	1.96	18.14	0.00	11.19	0.78	0.00	0.10	0.00
LN400		0.49	8.47	59.56	1.97	18.11	0.00	11.21	0.58	0.00	0.10	0.00
adipose		0.95	9.06	72.29	2.25	16.27	0.00	0.00	0.00	0.00	0.13	0.00
breast		0.98	8.59	70.10	2.33	17.90	0.00	0.00	0.00	0.00	0.13	0.95
solid water		1.02	8.00	67.29	2.39	19.87	0.00	0.00	0.00	0.00	0.14	2.31
Liver		1.09	8.06	67.01	2.47	20.01	0.00	0.00	0.000	0.000	0.14	2.31
brain		1.05	10.83	72.54	1.69	14.86	0.00	0.00	0.00	0.00	0.08	0.00
CB2-30%		1.33	6.68	53.47	2.12	25.61	0.00	0.00	0.00	0.00	0.11	12.01
CB2-50%		1.56	4.77	41.61	1.52	32.00	0.00	0.00	0.000	0.00	0.08	20.02
SB3 bone		1.82	3.41	31.41	1.84	36.49	0.00	0.00	0.00	0.00	0.04	26.81
B200 bone		1.15	6.65	55.51	1.98	23.64	0.00	0.00	0.00	3.24	0.11	8.87
IB3 bone		1.14	6.67	55.65	1.96	23.52	0.00	0.00	0.00	3.23	0.11	8.86
Lung(Inhale)		0.20	8.80	67.50	3.50	18.60	0.00	0.00	0.00	0.00	1.60	0.00
Adipose		0.96	10.00	71.30	1.80	16.40	0.00	0.00	0.000	0.00	0.20	0.30
Breast		0.99	9.60	70.30	1.90	17.00	0.00	0.00	0.000	0.00	0.20	0.90
Dense Bone	CIRS062	1.53	5.70	40.80	1.00	25.90	0.30	0.000	0.00	8.30	0.10	17.90
Liver		1.07	9.00	69.40	2.10	17.10	0.00	0.000	0.00	0.00	0.10	2.20
Muscle		1.06	9.10	69.70	2.10	16.80	0.00	0.00	0.00	0.00	0.10	2.20
Trabecular Bone		1.16	7.00	56.30	2.00	22.700	0.00	0.00	0.00	3.30	0.20	8.50
Lung(Exhale)		0.51	8.90	66.00	2.40	20.40	0.00	0.00	0.00	0.00	0.60	1.70

*the physical density of materials, SI: g/cm

equivalent materials can be calculated by the following formulas (1)–(3):

$$\rho_e = \frac{n_{e,M}}{n_{e,w}} = \frac{\varrho_M N_A \sum_i \omega_i \frac{Z_i}{A_i}}{\varrho_w N_A \sum_i \omega_i \frac{Z_i}{A_i}\,(w)} \tag{1}$$

$$\ln I = \left(\sum \frac{\omega_i Z_i}{A_i} \ln I_i\right)\left(\sum \frac{\omega_i Z_i}{A_i}\right)^{-1} \tag{2}$$

$$SPR_w = \rho_e{}^* \frac{\ln\left(\frac{2m_e c^2 \beta^2}{I(1-\beta^2)}\right) - \beta^2}{\ln\left(\frac{2m_e c^2 \beta^2}{I_w(1-\beta^2)}\right) - \beta^2} \tag{3}$$

where $\varrho_{M/w}$ is the density of the materials or water; N_A is Avogadro's number; ω_i is the mass fraction of the i-th element; Z and A are the atomic number and atomic weight of element, respectively. The elemental I-values were taken from ICRU Report 49 [30] and I_w is 75 eV. m_e is the mass of electron; β is the relative velocity of the incident particle, and in this article, the particle is a 200 MeV proton beam.

120 kVp CT images of the two phantoms were obtained, and the Gammex467 phantom data were used to establish the corresponding curve of CT number and SPR_w. The SPR_w of the inner and outer layers of the CIRS062 phantom could be obtained from this curve. Because the MAR algorithm can only be applied in GSI scan mode in GE Revolution CT. To evaluate the improvement effect of the MAR algorithm on metal artifacts, we used 120 kVp-like MonoE-CT images as the SECT method for predicting the SPR_w of materials in this study. We found that the MonoE-80 keV CT images were very close to the 120 kVp images in predicting the SPR_w of materials. So in this article, the MonoE-80 keV CT images were used as the 120 kVp-like CT images.

Dual-energy computer tomography method

Hunemohr established a three-step method of DECT-based SPR_w prediction [31]. The first step is to obtain the relative electron density (ρ_e) and effective atomic number (Z_{eff}) images by DECT:

$$\rho_e = a^* \left(\frac{HU_L}{1000} + 1\right) + (1 - a) * \left(\frac{HU_H}{1000} + 1\right) \tag{4}$$

$$Z_{eff} = \sqrt[1/3.1]{\rho_e{}^{-1*}\left(b^*\left(\frac{HU_L}{1000}+1\right) + \left(Z_{eff,w}^{3.1} - b\right) * \left(\frac{HU_H}{1000} + 1\right)\right)} \tag{5}$$

a, b are the fitting parameters, $HU_{L/H}$ represents the CT numbers obtained by different X-ray energies, and $Z_{eff,w}$ is the effective atomic number of water.

Then, an empirical relation, established by Yang [13], is used to determine the I-value from the Z_{eff}. In this article, Z_{eff} and $\ln I$ had a linear relationship, the slope was 0.049 and the intercept was 3.834. Finally, the SPR_w values of the materials are calculated according to the Bethe-Bloch formula (3). In our study, for 40–80 keV CT images, parameters a and b were –0.228 and 2104.613, respectively.

Accuracy analysis

The effect of metal on CT numbers was shown by mean of deviation. In order to quantitatively analyze the impact of metal objects on SPR prediction, the mean absolute error (MAE) and root mean squared

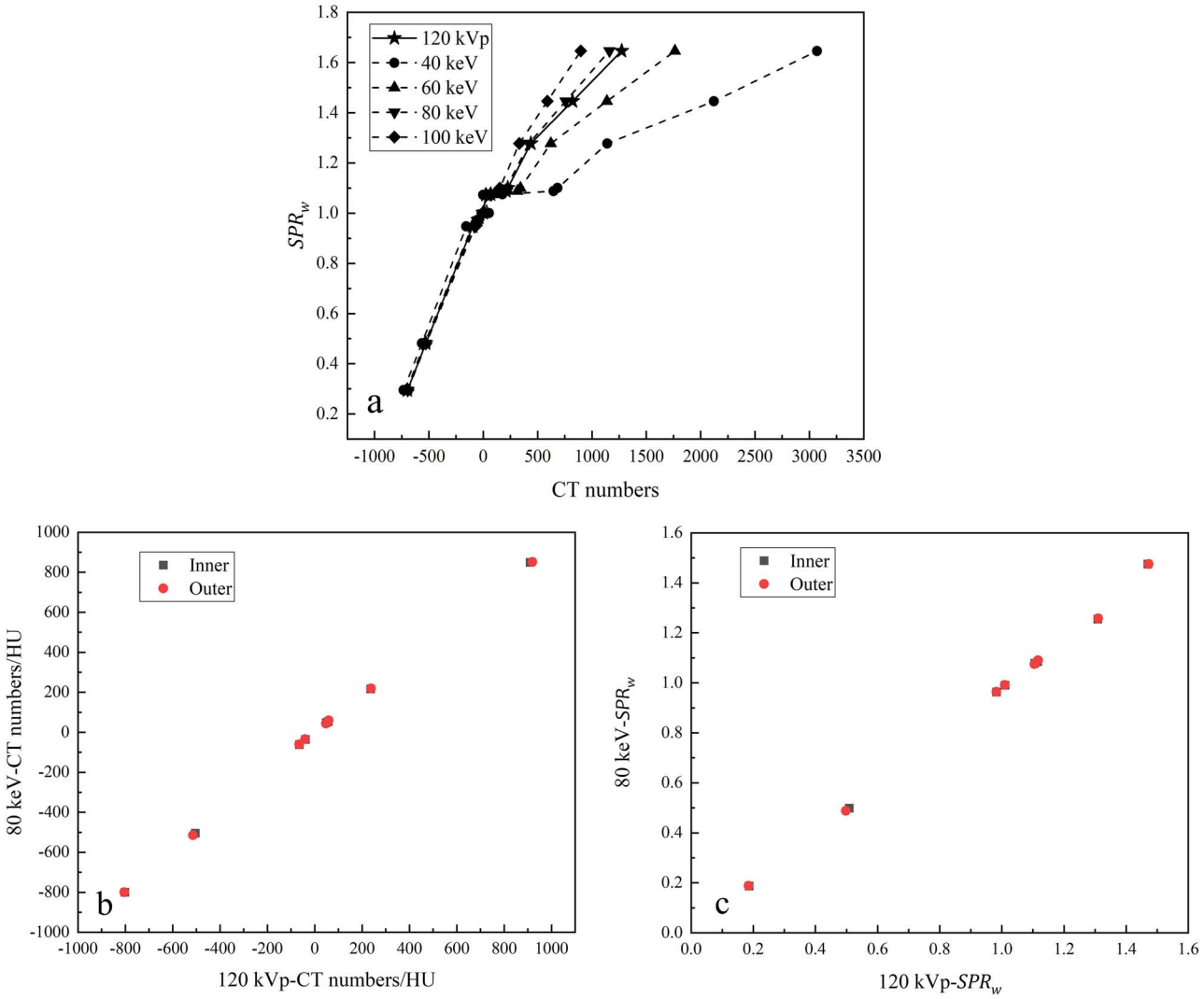

Fig. 2. a. Calibration curves between the CT numbers and the relative proton SPR to water. The CT number of air was set to −1000. b. The relationship between the CT numbers of 120 kVp and 80 keV images. c. The abscissa is the CIRS062 phantom SPR_w predicted by the 120 kVp CT images, and the ordinate is the phantom SPR predicted by the 80 keV CT images.

error (RMSE), defined below, were evaluated at 200 MeV proton energy:

$$\text{mean of deviation } (\%) = 100 \times \frac{\sum_{i=1}^{N} \frac{CT_{metal} - CT_{no\ metal}}{CT_{no\ metal}}}{N} \quad (6)$$

$$\text{MAE } (\%) = 100 \times \left(\frac{\sum_{i=1}^{N} \left| \frac{Est.SPR_i - Ture.SPR_i}{True.SPR_i} \right|}{N} \right) \quad (7)$$

$$\text{RMSE } (\%) = 100 \times \sqrt[2]{\frac{\sum_{i=1}^{N} \left(\frac{Est.SPR_i - True.SPR_i}{True.SPR_i} \right)^2}{N}} \quad (8)$$

$Est.SPR_i$ is the SPR of *i*-th tissue equivalent material predicted by SECT or DECT. $Ture.SPR_i$ is the theoretical value of SPR for this tissue equivalent material.

RESULTS

120 kVp and MonoE-80 keV images

We compared the calibration curves of CT number and SPR_w between 120 kVp CT images and four different MonoE-CT images, as shown in Fig. 2a. It can be seen that in the low density area (HU ≤ 200 HU), the five curves were essentially coincident, while in the high density area, there was some offset between the five curves. Among them, the CT − SPR_w calibration curve of MonoE-80 keV is the closest to 120 kVp.

For the tissue equivalent material of the inner layer of CIRS062, the maximum difference between the CT numbers obtained at 120 kVp and 80 keV was 61 HU, the maximum relative deviation was 8.86% and the average deviation was 5.06%. For the outer layer material, the maximum difference between the CT values of the two ray energies was 67 HU, the maximum relative deviation was 12.50% and the average deviation was 5.32% (Fig. 2b). SPR_W prediction results showed that

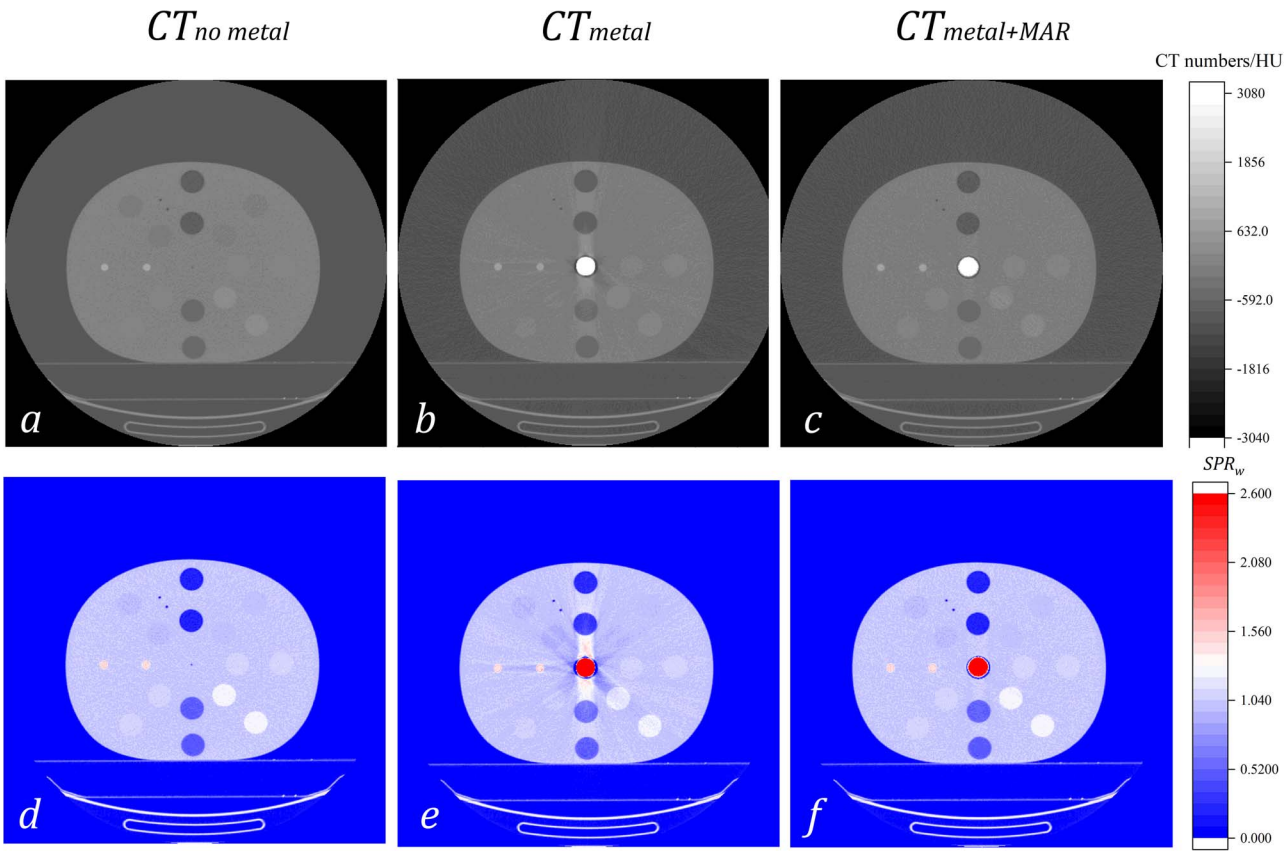

Fig. 3. Prediction of SPR_w of CIRS062 phantom using SECT method based on MonoE-80 keV CT images. The top three figures represent the CT images of CIRS062 in different scan mode, (a) $CT_{no\ metal}$ (b) CT_{metal} (c) $CT_{metal+MAR}$. The bottom three figures are the SPR_w images of the phantom predicted by the HU-SPR corresponding curve (SECT) in this scan mode, (d) $CT_{no\ metal}$ (e) CT_{metal} (f) $CT_{metal+MAR}$.

the average difference between 120 kVp and 80 keV was 1.89% (Inner) and 1.59% (Outer), as shown in Fig. 2c.

The impact of metal on SPR_w prediction and metal artifact reduction

Single-energy calculation method

The 80 keV CT images were used in the SECT. For the eight inserts located in the inner layer of the CIRS062 phantom, the mean of deviation between CT numbers with and without a titanium alloy femoral head was −14.47% (−63.83% to 19.44%), and the RMSE was 29.02%. Except for Lung inserts, the CT numbers of tissue equivalent materials were reduced when metal was present. The most affected insert was Muscle, for which the CT number was reduced by 63.83%, followed by Trabecular Bone. Dense Bone and Liver were the least affected by metal. For the outer layer, tissue-equivalent materials were less affected by metal. The mean of deviation of CT numbers was −2.86% (−12.33% to 11.43%), and the RMSE was 8.19%. Trabecular Bone was the tissue equivalent material whose CT number was most affected in the outer layer inserts. After using the MAR algorithm, compared with the case without metal, the mean CT number deviation of each insert in the inner layer was −0.97%, and the outer layer was −0.50%, as shown in Fig. 3a.

The SPR_w maps calculated from the 80 keV CT images of the three groups were shown in Fig. 3b. The SPR_w prediction results based on the calibration curve showed that when there was no metal ($CT_{no\ metal}$), the MAE of SPR_w of the inner and outer layers inserts were 3.19% and 3.43%, and the RMSE were 4.80% and 5.02%, respectively. When the metal was present (CT_{metal}), the MAE of SPR_w of the inner and outer layers was 13.88% and 5.42%, corresponding RMSE was 28.22% and 8.75%, respectively. Using the MAR algorithm ($CT_{metal+MAR}$), the MAE of SPR_w of inserts in the inner and outer layers reduced to 2.71% and 3%, respectively. The greatest impact on the SPR_w prediction of inner layer inserts with metal existence was the Lung equivalent materials, the SPR_w of which were largely overestimated. For Lung (Inhale), SPR_w increased by 76.65% and for Lung (Exhale), SPR_w increased by 21.30%. However, for the outer layer, Lung (Inhale) and Trabecular Bone received a greater impact, and the SPR_w increased by 21.98% and 10.05%, respectively.

Dual-energy calculation method

In GSI scan mode, the MonoE-40 and 80 keV CT images of the CIRS062 phantom were reconstructed. The CT numbers of the three groups are shown in Table 2. Metal had a greater impact on the CT numbers of low energy X-rays (40 keV), and the maximum difference

Table 2. The CT numbers (HU) of the CIRS062 electron density phantom in two monochromatic X-Rays reconstructed

Materials	Phantom	40 KeV				80 KeV	
		$CT_{no\ metal}$	CT_{metal}	$CT_{metal+MAR}$	$CT_{no\ metal}$	CT_{metal}	$CT_{metal+MAR}$
Lung(Inhale)	Inner	−855	−500	−827	−801	−653	−794
Adipose		−132	−154	−136	−62	−71	−63
Breast		−64	−84	−71	−36	−43	−35
Dense Bone		2379	2112	2303	849	788	830
Liver		100	73	98	53	51	56
Muscle		94	26	90	47	17	46
Trabecular Bone		681	489	646	216	142	209
Lung(Exhale)		−543	−239	−497	−505	−393	−486
Lung(Inhale)	Outer	−843	−738	−835	−800	−754	−797
Adipose		−132	−149	−133	−61	−66	−61
Breast		−68	−85	−71	−35	−39	−35
Dense Bone		2329	2221	2382	852	808	849
Liver		107	86	95	59	56	56
Muscle		86	78	92	44	41	46
Trabecular Bone		678	604	666	219	192	216
Lung(Exhale)		−547	−435	−530	−515	−477	−508

Table 3. The predicted range error of two proton beam energies in three scanning modes

Range error (mm)	no metal		metal		metal+MAR	
	Inner	Outer	Inner	Outer	Inner	Outer
100 MeV	1.01	0.99	3.76	1.15	1.34	0.73
200 MeV	3.31	3.30	12.69	3.88	4.48	2.40

in CT numbers caused by metal reached 355 HU. For 80 keV X-rays, the maximum difference in CT numbers was 148 HU. Hunemohr *et al* confirmed that the current algorithm could not be used to calculate the electron density of Lung tissue [14]; therefore, the calculation result of the Lung (Inhale) insert was excluded in this section. Using formulas (4)–(5), we obtained the relative electron density (ρ_e), effective atomic numbers (Z_{eff}) and SPR (SPR_w) images of the CIRS062 phantom in the three groups, as shown in Fig. 4.

For the $CT_{no\ metal}$ group, the MAE of ρ_e calculated by the DECT method was 1.02% and 1.13%, and the RMSE was 1.40% and 1.79%, respectively. The former was the inner layer, and the latter was the outer layer. The MAE of Z_{eff} was 6.09% and 5.71%, and the RMSE was 6.53% and 5.96%, respectively. For SPR_w, the MAE was 1.30% and 1.34%, and the RMSE was 1.60% and 1.90%, respectively.

For the CT_{metal} group, the MAE of the ρ_e calculated by DECT increased to 3.69% and 1.23%, and the RMSE were 5.94% and 1.57%, respectively. The MAE of Z_{eff} was 7.13% and 4.93%, and the RMSE was12.05% and 6%, respectively. The MAE of the predicted SPR_w was 3.69% and 1.36%, and the RMSE was 5.46% and 1.60%, respectively.

For the $CT_{metal+MAR}$ group, the MAE of ρ_e of the inner and outer layers of the CIRS062 phantom reduced to 1.23% and 0.84%, respectively, and the RMSE was 1.75% and 1.32%, respectively. The MAE of Z_{eff} was reduced to 4.30% and 4.78%, and the RMSE was 4.72% and 5.01%. The MAE of SPR_w predicted by DECT decreased to 1.46% and 1.05%, and the RMSE decreased to 1.86% and 1.44%, respectively.

The relative deviations of ρ_e, Z_{eff} and SPR_w of the CIRS062 phantom calculated by DECT methods from their theoretical values are shown in Fig. 5. It could be seen that the SPR_w of the same inserts in the inner and outer layers were almost the same without metal ($CT_{no\ metal}$), except for 'Dense Bone' and 'Lung (Exhale).' When the metal was present in the center of the phantom (CT_{metal}), the SPR_w of the inner inserts were more affected. The interval graph (Fig. 5d) clearly showed that the presence of metal would reduce the accuracy of SPR_w predictions, and the MAR algorithm could reduce this error to a certain extent.

DISCUSSIONS

Metal implants cause high X-ray attenuation, so artifacts appear in reconstructed CT image [32]. The interface between the implant and surrounding tissue is distorted, and the metal implant area is shown as high attenuation and low attenuation strip artifacts on the CT image

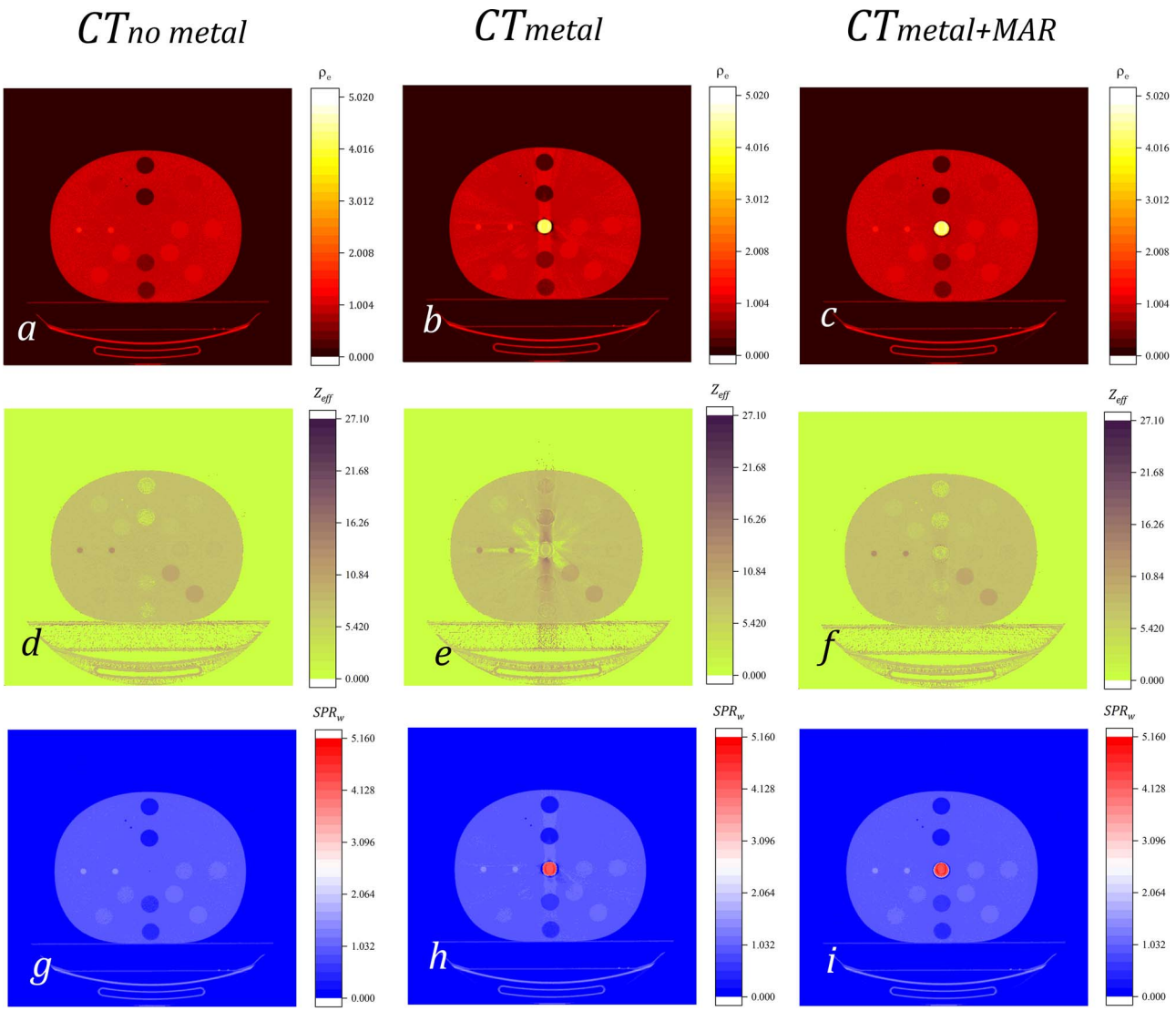

Fig. 4. The ρ_e, Z_{eff} and SPR_w images obtained by DECT method based on two energy CT images of 40-80 keV. (a)–(c): ρ_e, (d)–(f): Z_{eff}, (g) — (i) : SPR_w.Left is the$CT_{no\ metal}$ group. Middle is the CT_{metal} group. Right is the $CT_{metal+MAR}$ group.

[33, 34]. Therefore, higher image noise will also be present. The proton treatment planning system is more sensitive to changes in CT images, and the appearance of image artifacts will cause a non-negligible change in the dose distribution of proton therapy. In this study, we found that the presence of metal could reduce the prediction accuracy of SPR_w, while the MAR algorithm could mitigate the impact of metal objects on SPR_w prediction.

The 120 kVp is the X-ray energy commonly used in clinical CT scans. Figure shows that the 80 keV CT images could reflect the images of 120 kVp to a certain extent. Studies have shown that virtual MonoE-CT images can reduce the beam hardening effect [35, 36], which suggests that MonoE-CT images are more accurate in predicting the SPR_w of materials in the presence of metal objects than kVp images. The mean of deviations of SPR_w between the above two X-ray energies were 1.89% (−0.33% to 4.12%, inner) and 1.59% (−1.93% to 3.96%, outer), respectively. The MAE of SPR_w obtained by 120 kVp CT images were 4.47% and 4.84%, which were worse than MonoE-80 keV images (3.19% and 3.43%).

For the method of predicting material SPR_w by SECT (MonoE-80 keV), the MAE of SPR_w of the inner layer of the CIRS062 phantom was 3.19%, and the MAE was 3.43% for the outer layer ($CT_{no\ metal}$). The MAE increased to 13.88% and 5.42%, respectively, when a metal femoral head was placed in the center of the phantom (CT_{metal}). The metal impact on theSPR_w prediction of a material is distance dependent, and the closer to the metal, the greater impact on the SPR_w prediction. The presence of metal would underestimate the SPR_w of inner layer inserts, except for lung equivalent inserts. For outer layer inserts, the difference was that the SPR_w of 'Adipose' inserts would be overestimated and 'Lung (Exhale)' would be underestimated.

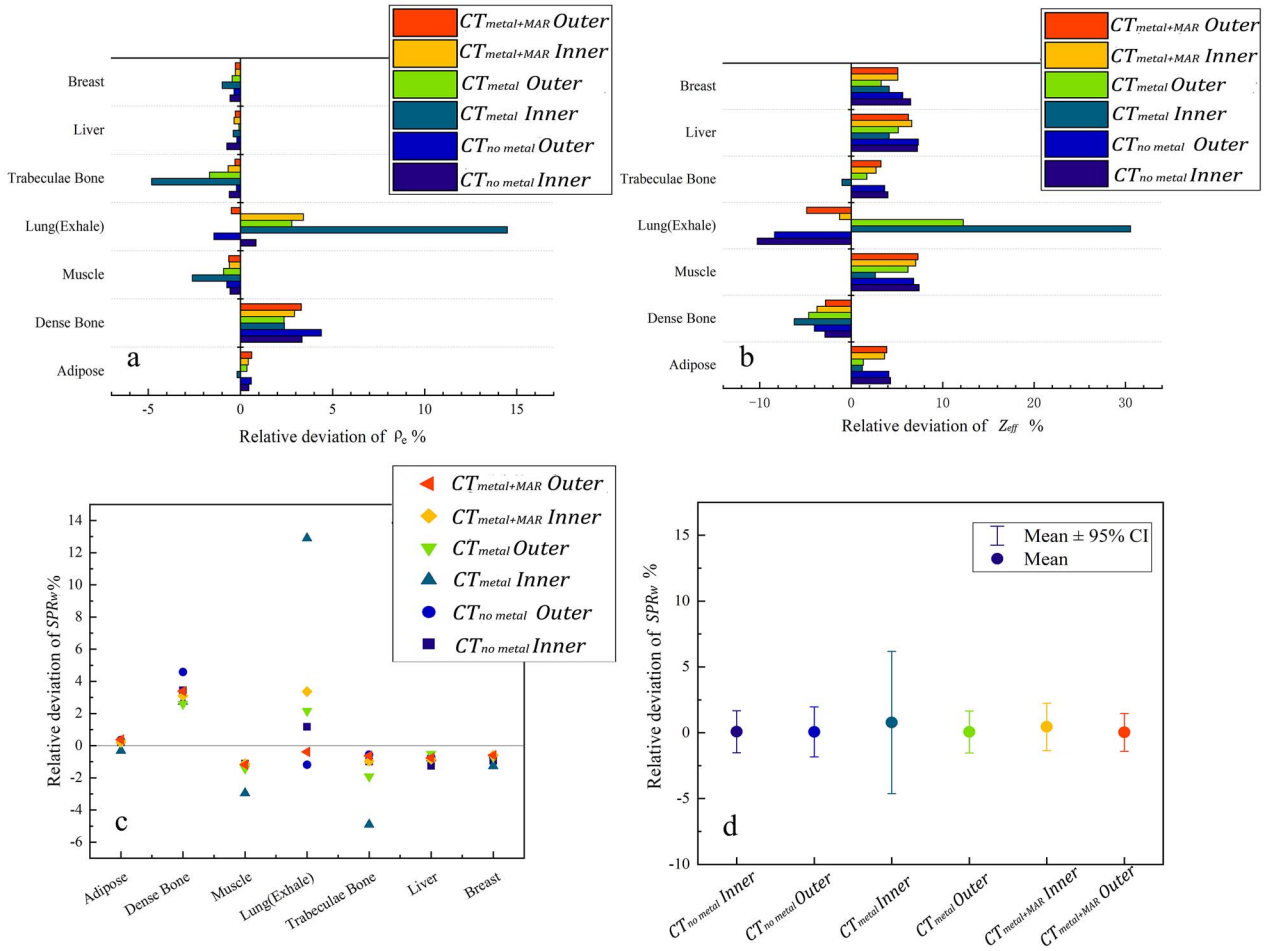

Fig. 5. a. The relative deviation between the relative electron density (ρ_e) of inserts of CIRS062 phantom calculated by the DECT method and the theoretical value. b. The relative deviation between Z_{eff} calculated by DECT and the theoretical value. c. The relative deviation of the SPR_w of different inserts of the CIRS062 phantom calculated by the DECT method in the three groups. d. The interval graph of the SPR_w prediction results of the CIRS062 phantom.

Using the MAR algorithm could significantly reduce the bias of SPR_w prediction; the MAE of SPR_w for the inner layer inserts was reduced to 2.71%, and the MAE of the outer layer inserts was 2.99% ($CT_{metal+MAR}$). The MAE of the predicted SPR_w for the CIRS062 phantom was even slightly better than that in the absence of metal.

The SPR_w of materials predicted by the DECT method is more accurate than those predicted by the SECT method, and the prediction accuracy of theSPR_w is improved by approximately 2%. Moreover, the SPR_w predicted by the DECT method is less affected by the metal. When a metal was present at the center of the CIRS062 phantom, the SPR_w prediction deviation of the inner layer insert was only increased to 3.69% compared with those without metal. For the outer layer inserts, the MAE of SPR_w did not change significantly compared to the metal-free case. We did not calculate the SPR of 'Lung (Inhale)' due to the limitations of this DECT method. The results showed that the presence of metal (CT_{metal}) would overestimate the SPR_w of the 'Lung (Exhale)' and 'Liver' inserts and underestimate the rest of the inserts for both the inner layer and outer layer. For the inner layer inserts, the most affected insert was 'Trabecular Bone,' followed by 'Muscle.' For outer layer inserts, the most affected insert was 'Dense Bone,' followed by 'Trabecular Bone.' Based on the spatial positions of the individual inserts around the metal, we suspected that the metal may have a greater impact on the materials behind the metal than the material in front.

For proton therapy, the primary concern of physicians and physicists is the effect of metal artifacts on beam range. We calculated the range of 100 MeV and 200 MeV proton beams in each tissue equivalent material in three cases using the DECT method. The results are shown in Table 3.

It can be seen that the metal object had a great impact on the prediction of the range in tissue equivalent material of the nearby. When there is a metal, the range prediction error of the equivalent material in the inner layer of the CIRS062 phantom is increased by nearly three times compared with that without metal. While with MAR algorithm, the calculation accuracy of the range of tissue materials around metal objects can be significantly improved.

The X-ray attenuation of a material is not only dependent on its density but also the energy of the X-rays. For each material, the energy dependence in the attenuation absorption is specific to the atomic number [14]. Therefore, different materials with the same CT number under a single X-ray energy can be distinguished under DECT. The DECT index (DEI) can quantify this differentiation. It is defined as [32]:

$$\mathrm{DEI} = \mathrm{HU_L} - \mathrm{HU_H}/\mathrm{HU_L} + \mathrm{HU_H} + 2000 \quad (9)$$

In this article, DEI was used to evaluate the influence of metal on the DECT images. When there was no metal ($CT_{no\ metal}$), the mean DEI of the eight inserts of the inner and outer layers were 0.031 and 0.034. When there was metal in the center of the phantom (CT_{metal}), the mean DEI of the inner and outer layers were 0.08 and 0.057. After reconstruction with the MAR algorithm ($CT_{metal+MAR}$), the mean DEI were 0.040 and 0.038. DEI is related to the atomic number of the materials. The results of the study showed that the presence of metal would cause a significant change in DEI, which indicated that DECT would incorrectly estimate the Z_{eff} of materials when there was metal, and the MAR algorithm could reduce the degree of incorrect estimation (Fig. 5b). The two-step DECT method in this article predicts the SPR_w of a material needed to obtain the Z_{eff} of the material first. The DEI results suggested that the inaccuracy of the Z_{eff} calculation may affect the accuracy of the SPR_w predictions due to the presence of metals.

Our study showed that for both SECT and DECT methods, the MAR algorithm could significantly improve the prediction accuracy of the SPR_w of a material with metals. Therefore, the MAR algorithm in CT scans was recommend when cancer patients with metal implants in particle therapy.

However, this study also has a few limitations. First, the metal object used in this study was only a hemispherical titanium alloy femoral head; other types and materials implants were not included. Second, our study was a quantitative study of the phantom, and the impacts of high and low attenuation artifacts caused by metal on the surrounding tissues and organs *in vivo* were not evaluated. Therefore, more research is needed to analyze the effect of metal implants in the human body on the prediction of tissue SPR_w.

CONCLUSION

In this article, the CIRS062 electron density phantom was used to evaluate the stopping power ratios in the presence of metal predicted by both SECT and DECT methods, respectively. Our results show that the DECT method is significantly less affected by metal when predicting the SPR of tissue substitutes. The SPR of the tissue equivalent materials behind the metal is more affected. The MAR algorithm can significantly improve the prediction accuracy of the SPR of tissues in the presence of metal.

FUNDING

This work was supported by the 1.3.5 for Disciplines of excellence-Clinical Research Incubation Project, West China Hospital, Sichuan University (2021HXFH029), and the Science and Technology Support Program of Sichuan Province, China (No.2021YFQ0065)

CONFLICT OF INTEREST

The authors have no conflicts of interest to disclose.

REFERENCES

1. Vaishnav JY, Ghammraoui B, Leifer M et al. CT metal artifact reduction algorithms: Toward a framework for objective performance assessment[J]. *Med Phys* 2020;47:3344–55.
2. Ziemann C, Stille M, Cremers F et al. Improvement of dose calculation in radiation therapy due to metal artifact correction using the augmented likelihood image reconstruction[J]. *J Appl Clin Med Phys* 2018;19:227–33.
3. Man BD, Nuyts J, Dupont P et al. Metal streak artifacts in X-ray computed tomography: a simulation study[J]. *IEEE Trans Nucl Sci* 2002;46:691–6.
4. Man BD, Nuyts J. Reduction of metal streak artifacts in X-ray computed tomography using a transmission maximum a posteriori algorithm[J]. *IEEE Trans Nucl Sci* 2000;2:977–81.
5. Huang JY, Kerns JR, Nute JL et al. An evaluation of three commercially available metal artifact reduction methods for CT imaging[J]. *Phys Med Biol* 2015;60:1047–67.
6. Andersson KM, Christina VD, Johan R et al. Evaluation of two commercial CT metal artifact reduction algorithms for use in proton radiotherapy treatment planning in the Head & Neck area[J]. *Med Phys* 2018;45:4329–44.
7. U.S. Food and Drug Administration. *510(k) Premarket Notification: Revolution CT*. https://www.accessdata.fda.gov/scripts/cdrh/cfdocs/cfpmn/pmn.cfm?ID=K163213 (23 May 2022, data last accessed).
8. U.S. Food and Drug Administration. *510(k) Premarket Notification: Philips Ingenuity CT*. https://www.accessdata.fda.gov/scripts/cdrh/cfdocs/cfpmn/pmn.cfm?ID=K160743 (23 May 2022, data last accessed).
9. U.S. Food and Drug Administration. *510(k) Premarket Notification: iMAR*. https://www.accessdata.fda.gov/scripts/cdrh/cfdocs/cfpmn/pmn.cfm?ID=K142584 (23 May 2022, data last accessed).
10. Schneider U, Pedroni E, Lomax A. The calibration of CT Hounsfield units for radiotherapy treatment planning[J]. *Phys Med Biol* 1996;41:111–24.
11. Yang M, Zhu XR, Park PC et al. Comprehensive analysis of proton range uncertainties related to patient stopping-power-ratio estimation using the stoichiometric calibration[J]. *Phys Med Biol* 2012;57:4095–115.
12. Paganetti H. Range uncertainties in proton therapy and the role of Monte Carlo simulations[J]. *Phys Med Biol* 2012;57:99–117.
13. Yang M, Virshup G, Clayton J et al. Theoretical variance analysis of single- and dual-energy computed tomography methods for calculating proton stopping power ratios of biological tissues[J]. *Phys Med Biol* 2010;55:1343–62.
14. Hünemohr N, Krauss B, Dinkel J et al. Ion range estimation by using dual energy computed tomography.[J]. *Z Med Phys* 2013;23:300–13.
15. Masatoshi S. Potential of dual-energy subtraction for converting CT numbers to electron density based on a single linear relationship[J]. *Med Phys* 2012;39:2021–30.

16. Möhler C, Wohlfahrt P, Richter C, Greilich S. Range prediction for tissue mixtures based on dual-energy CT[J]. *Phys Med Biol* 2016;61:N268–N75.
17. Pessis E, Campagna R, Sverzut JM et al. Virtual monochromatic spectral imaging with fast kilovoltage switching: reduction of metal artifacts at CT.[J]. *Radiographics* 2013;33:573–83.
18. Katsura M, Sato J, Akahane M et al. Current and Novel Techniques for Metal Artifact Reduction at CT: Practical Guide for Radiologists[J]. *J Infect Dis* 1980;34:450–61.
19. Wellenberg R, Hakvoort ET, Slump CH et al. Metal artifact reduction techniques in musculoskeletal CT-imaging[J]. *Eur J Radiol* 2018;107:60–9.
20. Gauntt DM. A suggested method for setting up GSI profiles on the GE Revolution CT scanner[J]. *J Appl Clin Med Phys* 2019;20:169–79.
21. Schmidt B, Flohr T. Principles and applications of dual source CT[J]. *Phys Med* 2020;79:36–46.
22. Sakabe D, Funama Y, Taguchi K et al. Image quality characteristics for virtual monoenergetic images using dual-layer spectral detector CT: Comparison with conventional tube-voltage images[J]. *Phys Med* 2018;49:5–10.
23. Kidoh M, Nakaura T, Nakamura S et al. Reduction of dental metallic artefacts in CT: Value of a newly developed algorithm for metal artefact reduction (O-MAR)[J]. *Clin Radiol* 2014;69:e11–6.
24. Li H, Noel C, Chen H et al. Clinical evaluation of a commercial orthopedic metal artifact reduction tool for CT simulations in radiation therapy[J]. *Med Phys* 2012;39:7505–17.
25. Annkah JK, Rosenberg I, Hindocha N et al. Assessment of the dosimetric accuracies of CATPhan 504 and CIRS 062 using kV-CBCT for performing direct calculations[J]. *Journal of Medical Physics* 2014;39:133–41.
26. Constantinou C. A solid water phantom material for radiotherapy x-ray and γ-ray beam calibrations[J]. *Med Phys* 1982;9:436–41.
27. White DR, Constantinou C, Martin RJ. Foamed epoxy resin-based lung substitutes. *Br J Radiol* 1986;59:787–90.
28. White DR, Martin RJ, Darlison R. Epoxy resin based tissue substitutes. *Br J Radiol* 1977;50:814–21.
29. Sun X, Zhao Q, Sun P et al. Metal artifact reduction using monoenergy images combined with metal artifact reduction software in spectral computed tomography: a study on phantoms[J]. *Quant Imaging Med Surg* 2020;10:1516–25.
30. ICRU. ICRU Report 49. Stopping Powers and Ranges for Protons and Alpha Particles. *International Commission on Radiation Units and Measurements* 1993;94:014557.
31. Hünemohr N, Krauss B, Tremmel C et al. Experimental verification of ion stopping power prediction from dual energy CT data in tissue surrogates.[J]. *Phys Med Biol* 2014;59:7081–4.
32. Lee MJ, Kim S, Lee SA et al. Overcoming artifacts from metallic orthopedic implants at high-field-strength MR imaging and multidetector CT[J]. *Radiographics A Review Publication of the Radiological Society of North America Inc* 2015;27:791.
33. Andersson KM, Nowik P, Persliden J et al. Metal artefact reduction in CT imaging of hip prostheses—an evaluation of commercial techniques provided by four vendors.[J]. *Br J Radiol* 2015;88:20140473.
34. Stradiotti P, Curti A, Castellazzi G et al. Metal-related artifacts in instrumented spine. Techniques for reducing artifacts in CT and MRI: state of the art[J]. *Eur Spine J* 2009;18:102–8.
35. Yu L, Leng S, Mccollough CH. Dual-Energy CT–Based Monochromatic Imaging[J]. *AJR Am J Roentgenol* 2012;199:S9–S15.
36. Bamberg F, Dierks A, Nikolaou K et al. Metal artifact reduction by dual energy computed tomography using monoenergetic extrapolation[J]. *Eur Radiol* 2011;21:1424–9.